Planetary and Space Science 59 (2011) 319–326

Contents lists available at ScienceDirect

Planetary and Space Science

journal homepage: www.elsevier.com/locate/pss

Measurements of the terrestrial dust influx variability by the Cosmic Dust Experiment

Andrew Poppe [a,b,*], David James [a], Mihály Horányi [a,b]

[a] Laboratory for Atmospheric and Space Physics, UCB 392, University of Colorado, Boulder, CO 80309, USA
[b] Department of Physics, University of Colorado, 2000 Colorado Ave, Boulder, CO 80309, USA

ARTICLE INFO

Article history:
Received 7 October 2010
Received in revised form
16 November 2010
Accepted 2 December 2010
Available online 8 December 2010

Keywords:
Interplanetary dust
Terrestrial dust influx
Polar mesospheric clouds

ABSTRACT

We report on the results of the Cosmic Dust Experiment (CDE) onboard the Aeronomy of Ice in the Mesosphere (AIM) satellite, collected during eight months of operation between May 2007 and February 2008. CDE is an impact detector designed to measure the variability of the cosmic dust influx of grains with radius, $1.5 < r < 8$ μm. CDE consists of 14 permanently polarized polyvinylidene fluoride (PVDF) channels that produce an electrical signal when impacted with hyper-velocity dust particles. The instrument has a total surface area of 0.11 m^2 and a time resolution of 1 s. CDE experienced higher noise levels than expected on-orbit, triggering the need for new laboratory experiments, as well as the development of new data reduction approaches. We present the first eight months of reduced CDE data, highlighting the observed spatial and temporal variability of the cosmic dust influx.

1. Science background

A number of techniques have been used to measure the cosmic dust influx into our atmosphere, including high-powered large-array (HPLA) radars (Mathews et al., 2001; Janches and ReVelle, 2005; Sparks and Janches, 2009), optical observations (Hörz et al., 1975; Leinert, 1975) and in situ dust detectors (Love and Brownlee, 1993; Tuzzolino et al., 2001a; Schwanenthal, 2004). HPLA radar offers a unique window on micron-sized dust flux measurements by analyzing the meteor head echoes generated by dust particles undergoing ablation in Earth's upper atmosphere. Recent work has attempted to refine the physical description of ablating particles and their detection via radar (Fentzke and Janches, 2008), yet such measurements are by nature limited to observations at specific terrestrial latitudes. In situ dust detectors, such as the Long Duration Exposure Facility (LDEF) (Love and Brownlee, 1993) and the Space Dust (SPADUS) instrument aboard the ARGOS spacecraft (Tuzzolino et al., 2001a), have measured the terrestrial cosmic dust influx; however, significant uncertainty remains in the spatial and size distributions and variability thereof (Fig. 1). The estimates for the flux of particles < 10 μm in radius show disagreement on an order of magnitude, highlighting the difficulties of measuring the sub-millimeter dust flux.

Dust grains with radii on the order of 100 μm dominate the mass influx of cosmic material into the terrestrial atmosphere. These grains ablate to sub-nanometer-sized particles at an altitude of approximately 80–90 km, and re-condense to nanometer-sized smoke particles (Hunten et al., 1980; Kalashnikova et al., 2000; Rapp, 2009). The presence of these particles has been identified as a factor in various middle atmospheric phenomena, including Polar Mesospheric Clouds (PMC) (Turco et al., 1982; Rapp and Thomas, 2006), Polar Mesosphere Summer Echoes (PMSE) (Cho and Kelley, 1993; Cho and Röttger, 1997; Rapp and Lübken, 2001; Lübken and Rapp, 2001) and the formation of metallic layers (Plane, 2003). Ablation products from micrometeorites can also play a role in stratospheric physics (Turco et al., 1981; Murphy et al., 1998; Cziczo et al., 2001). Cosmic dust particles are a leading candidate for the creation of condensation nuclei (CN) for PMC and are believed to be responsible for creating electron bite-outs in the local plasma density, leading to PMSE. Recent models have shown that the eventual distribution of smoke particles in the mesosphere is highly sensitive to the amount and variability of the cosmic dust influx (Megner et al., 2008; Bardeen et al., 2008). Therefore, an accurate, temporally and spatially resolved measurement of the terrestrial cosmic dust input is critical in determining the role and extent of cosmic dust forcing on mesospheric phenomena.

2. Instrument description

The Cosmic Dust Experiment (CDE) is a polyvinylidene fluoride (PVDF) based impact-dust detector on the Aeronomy of Ice in the Mesosphere (AIM) satellite (Russell et al., 2009), a mission devoted

* Corresponding author at: Laboratory for Atmospheric and Space Physics, UCB 392, University of Colorado, Boulder, CO 80309, USA.
E-mail addresses: poppe@lasp.colorado.edu, Andrew.Poppe@lasp.colorado.edu (A. Poppe).

0032-0633/$ - see front matter © 2010 Elsevier Ltd. All rights reserved.
doi:10.1016/j.pss.2010.12.002

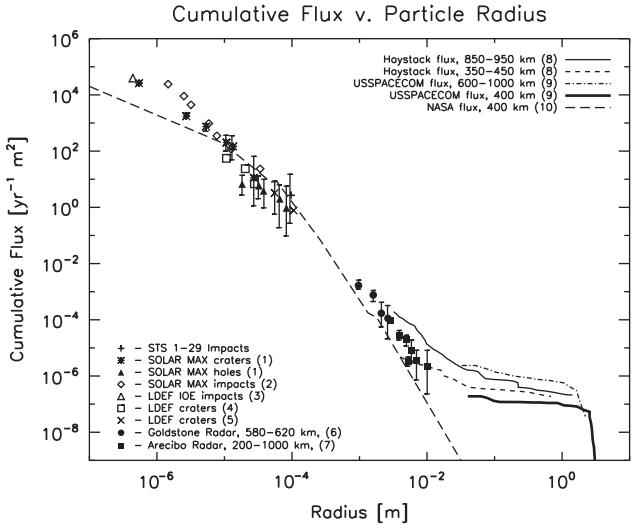

Fig. 1. Cumulative flux versus radius for terrestrial cosmic dust from a variety of measurements. Adapted from Gleghorn et al. (1995). References in the legend: (1)—NASA/JSC; (2)—Laurance and Brownlee (1986); (3)—Simon et al.; (4)—Bernhard et al.; (5)—Humes; (6)—Goldstein and Randolph (1992); (7)—Thompson et al. (1992); (8)—Stansbery et al. (1995).

to investigating PMC phenomena. CDE is nearly identical to the Student Dust Counter onboard the New Horizons mission to Pluto (Horányi, 2008; Poppe et al., 2010) and PVDF detectors have been previously flown on several spacecraft, including the Cassini mission to Saturn (Srama et al., 2004), the ARGOS mission around Earth (Tuzzolino et al., 2001a) and the STARDUST mission to comet 81P/Wild (Tuzzolino et al., 2004). PVDF is known to be mechanically and thermally stable, radiation resistant and non-responsive to energetic particle impacts, providing an ideal method for dust detection.

Similar to the Student Dust Counter, CDE consists of 14, 28 μm–thick PVDF detectors coated with 100 nm of aluminum–nickel and mounted to an external panel facing the zenith direction. Twelve of the detectors are exposed to space (referred to as the 'science' detectors), while two detectors are covered by aluminum cases and mounted to the underside of the instrument panel in order to detect background signals ('reference' detectors). When a dust particle impacts a detector, the AlNi layer is punctured and a crater is formed in the polarized PVDF, generating a fringing electric field around the crater (Poppe et al., 2010). This fringing electric field causes a change in the charge density on the AlNi plate, which is measured by an accompanying electronics box mounted to the inside of the AIM spacecraft. The total number of electrons, N, generated by an impacting dust particle was empirically fit based on experimental calibration data (Simpson and Tuzzolino, 1985; Tuzzolino, 1992; James et al., 2010) and is given by

$$N = (1.2 \times 10^{15} + 6.7 \times 10^{12} \cdot T) \cdot v^{2.88} \cdot m^{1.052}, \quad (1)$$

where v [km/s] is the impactor speed, m [g] is the impactor mass and T [°C] is the detector temperature. Since the charge is dependent on both the particle mass and velocity, it is assumed that the incoming particles are on radial trajectories with velocities equal to the Earth escape velocity. While previous work has shown that micrometeorites can enter the Earth's atmosphere at speeds significantly higher than the terrestrial escape velocity at 80–140 km (Janches et al., 2003, 2006; Sulzer, 2004; Janches and Chau, 2005), we follow previous work and assume the terrestrial escape velocity at CDE's orbit (600 km) (Hunten et al., 1980; Love and Brownlee, 1991; Kalashnikova et al., 2000). The escape velocity is vectorially added to the spacecraft velocity to calculate the dust impact speed. While space debris is present in the near-Earth environment, such particles would not significantly contribute to the CDE dataset. This is due to the fact that orbital debris are mainly circular orbits and therefore, would strike CDE at approximately 90° (Tuzzolino et al., 2001a, 2001b), outside CDE's sensitive range of impact angles of $< 45°$ (Horányi, 2008).

Using Eq. (1), the measured impact amplitude and the calculated impact velocity are used to determine the grain mass. CDE has a 1-s time resolution, a total surface area of 0.11 m^2 and can resolve dust grain masses within a factor of two for mass, $10^{-11} < m < 5 \times 10^{-9}$ g. CDE cannot resolve particle mass for grains with $m > 5 \times 10^{-9}$ g, yet still records an impact for these grains. The measured grain masses are converted into grain radii by assuming a spherical grain shape and a density of 2500 kg m^{-3} (Jessberger et al., 2001).

PVDF sensors are known to be susceptible to generating spurious signals, due to their piezo- and pyroelectric properties (Nalwa, 1995). For this reason, as in the case of SDC, we use the two underside-mounted detectors as noise-monitoring channels. The measured event rate on the science detectors is due to dust impacts and noise, while the rate on the reference detectors is due to noise only. The final dust flux is calculated by subtracting the reference event rate from the science event rate and normalizing by observation time and instrument area.

3. Initial data

The AIM spacecraft was launched out of Vandenberg AFB, California into a noon–midnight polar orbit on April 25, 2007 onboard a Pegasus rocket. CDE was first activated on May 25, 2007 and after an initial period of checkout and calibration, began nominal science observation on June 19, 2007. CDE operated nominally from June 19, 2007 to February 9, 2008, when the entire AIM spacecraft underwent a safing period for approximately one month. Following this safehold period, the noise levels increased dramatically on CDE, rendering later data unusable.

Upon analysis of the CDE data, several significant noise patterns were evident. Fig. 2 shows the time and solar zenith angle for 50 days of raw data from detector #8, which is a typical detector. These noise sources were unanticipated and serious enough to impede a straightforward analysis of the data. The noise can be divided into two categories based on geographical position and temporal behavior. The first of these noise sources occurs roughly in the range $-10° < \alpha < 60°$, where α is the solar zenith angle (SZA) of the AIM spacecraft. Given AIMs polar orbit, this SZA range corresponds

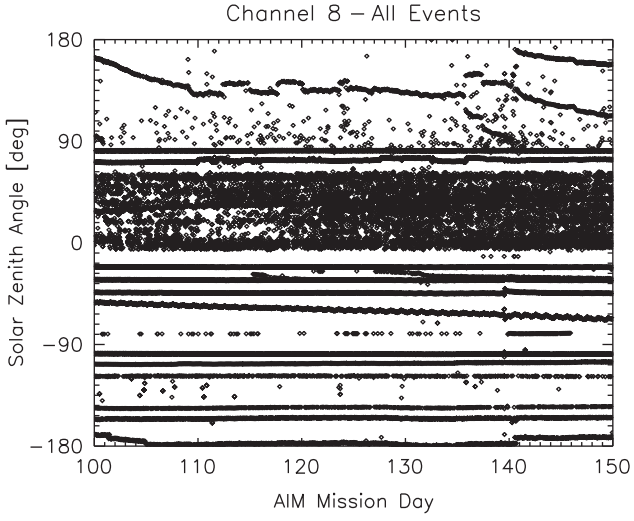

Fig. 2. Time versus solar zenith angle for all events on channel 8 for 50 consecutive days.

roughly to the sunward northern hemisphere. For any given orbit, the noise appears intermittently over a period of about 20 min. This noise does not significantly change from orbit to orbit and only occurs on the upward facing science channels and not on the reference detectors. The second category of noise consists of a collection of transient events at recurring latitudes. These events occur in sharp, sub-second bursts and are spatially coincident from orbit to orbit and therefore, as seen in Fig. 2, appear as lines. The lines drift slowly, yet occasionally show sharp changes in their behavior. This noise source appears on all detectors, both science and reference; however, some individual channels record additional lines not seen by any other channel. The population of events making up the lines often have Gaussian-shaped amplitude distributions, a fact which is exploited later in the noise reduction algorithm.

Initial attempts to ascertain the cause of the noise focused on interference from various spacecraft and instrument activities, such as spacecraft maneuvers, reaction wheel speeds, imaging sequences of the Cloud Imaging and Particle Size (CIPS) instrument (Rusch et al., 2009) and observations by the Solar Occultation for Ice Experiment (SOFIE) (Gordley et al., 2008). Thorough investigation of these types of spacecraft activities produced no correlations and therefore, alternative explanations for the noise were sought. For the noise occurring over the northern hemisphere, it was suggested that the pyroelectric nature of PVDF detectors (Nalwa, 1995) could be causing a current to flow as the detectors entered sunlight and rapidly warmed. Another hypothesis was that the increasing temperature of the PVDF detectors in the sunward northern hemisphere portion of the orbit could cause an increasing mis-match between the detector capacitance and the CSA input capacitance. Such a mis-match is known to decrease the signal-to-noise ratio of the detector (Radeka, 1974; Spieler, 2005; Horányi, 2008). The correlation of the northern hemisphere noise with the solar zenith angle provided circumstantial evidence that solar heating of the channels might be responsible for this noise. The results of subsequent laboratory experiments to characterize the production of this noise using the CDE spare detectors are discussed in Section 4.

For the line-type noise, thermal expansion and/or contraction between adjacent materials with different thermal properties on the spacecraft and/or the instrument could cause acoustic vibrations, to which the detectors are known to be susceptible due to their piezoelectric properties (Nalwa, 1995). Since the line noise occurs simultaneously across all 14 channels, the cause is most likely not individual detector components. Furthermore, the CDE instrument deck is designed to continuously flex under thermal deformation, making it also unlikely to be the source of sharp vibrations. A more likely candidate for this noise is a spacecraft component, such as the solar array assembly, undergoing thermally induced expansion and contraction. However, the multitude and complexity of the various components of the AIM spacecraft prevent the absolute identification of the component(s) causing the line noise on CDE. While descriptions of the nature and cause for the line noise cannot be completely developed and confirmed, this noise is easily identified. The methods for removing this noise from the data are discussed in Section 5.

4. Laboratory noise investigations

Two separate hypotheses were generated to explain the presence of the northern hemisphere noise: (1) the pyroelectric nature of the PVDF detectors caused a DC current to flow into the analog electronics, which was then interpreted as false hits, or (2) the detectors were heated during the sunlit portion of the orbit, causing the detector capacitance to increase drastically (shown as a function of temperature in Fig. 3). Capacitance mis-match between the PVDF detector and the CSA input capacitance is known to cause elevated levels of noise in the detector electronics (Radeka, 1974; Spieler, 2005; Horányi, 2008).

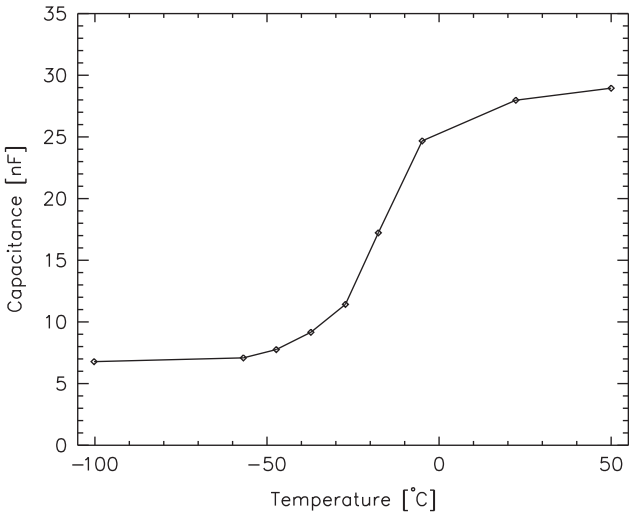

Fig. 3. The capacitance of a 28 μm PVDF detector as a function of temperature.

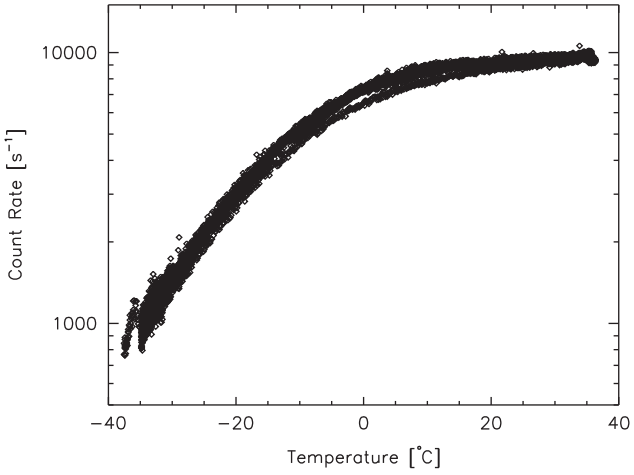

Fig. 4. The hit rate as a function of detector temperature, demonstrating the highly correlated nature of the count rate with the temperature.

In order to investigate and distinguish between these hypotheses, a spare flight detector was mounted to a $\frac{1}{4}$−inch aluminum plate that was heated by electric heaters or cooled by thermoelectric coolers and a chiller in order to simulate the orbital thermal environment. The temperature of the detector was measured by using a thermistor attached to the back of the detector. The detector was run through an extended series of heating and cooling cycles to simulate on-orbit temperatures ($\sim -35\ ^{\circ}\mathrm{C} < T < \sim +35\ ^{\circ}\mathrm{C}$) while the count rate was simultaneously measured. Figs. 4 and 5 show the measured hit rate as a function of the temperature and the temperature derivative, respectively. As is clearly seen, the noise rate is highly correlated with the detector temperature (and therefore, the detector capacitance) and uncorrelated with the derivative of the temperature. From these results, we conclude that the presence of the northern hemisphere noise is due to the increasing capacitance mis-match between the PVDF detector and the CSA input capacitance. This issue was unfortunately overlooked in the design transfer from the Student Dust Counter, which operated at

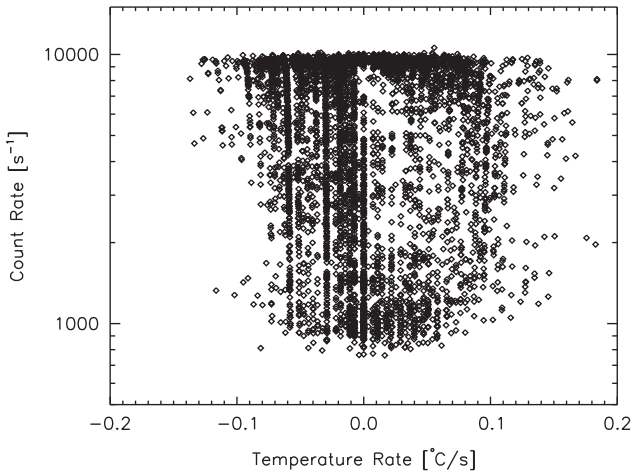

Fig. 5. The hit rate as a function of the derivative of the detector temperature, demonstrating the uncorrelated nature of the count rate with the derivative of the temperature.

much colder detector temperatures ($T \sim -95$ °C), to the Cosmic Dust Experiment, with detector temperatures of -35 °C $< T < +35$ °C.

5. Noise removal algorithms

In order to obtain the cosmic dust flux signal out of the raw CDE data, an ad-hoc yet rigorous algorithm was developed to recognize noise and remove it from the data. The noise reduction algorithm for CDE consists of two main parts, referred to as 1st Order (O1) and 2nd Order (O2). The O1 algorithm applies a series of four basic filters to the data to remove the most obvious noise events.

1. Temporal coincidence: the temporal coincidence filter removes any events occurring simultaneously ($\Delta t < 1$ s) across one or multiple channels. The anticipated dust flux is low enough that the probability of two dust particles impacting simultaneously is negligible and therefore, any two coincident events are assumed to be noise.
2. Spatial coincidence: the spatial coincidence filter removes any events that occur within 0.25° of another hit on consecutive orbits. This filter was motivated by the unique nature of noise lines seen in the CDE data, which appear consistently in latitude over long periods of time and the low probability that two dust impacts on sequential orbits would be at the same point in SZA.
3. Northern hemisphere filter: the northern hemisphere filter removes all events generated during the northern hemisphere portion of the orbit contaminated by the noise discussed in Section 4. The amount of noise in this period ($-10° < \alpha < +60°$) is so great that the data cannot be reduced.
4. Mask filter: the mask filter removes anomalous periods of data corresponding to easily recognizable instrument artifacts, such as internal CDE calibrations and special experiments conducted by the CIPS instrument which disrupt CDE measurements.

Events removed by the O1 filters listed above are collectively termed coincident events, while all events remaining are called 'candidate hits.' Fig. 2 shows all events for channel 8 for 50 days, while Fig. 6 shows the candidate hits for the same channel during the same period.

The 2nd Order noise algorithm for CDE is of a finer nature than the 1st Order. Upon investigation of the candidate hits, lines were still visually identifiable (see Fig. 6, $\alpha \sim -120°$), implying that the O1 filters were not thoroughly removing the line noise. Thus, the main goal of the O2 reduction code is to remove noise line events

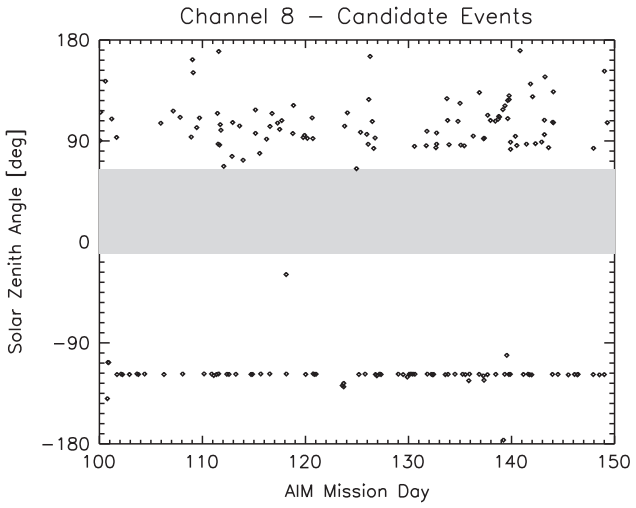

Fig. 6. Candidate hits on channel 8 for the same time period as Fig. 2. The northern hemisphere noise region has been grayed out for reference. A noise line in the candidate data is still evident at a solar zenith angle of $-120°$.

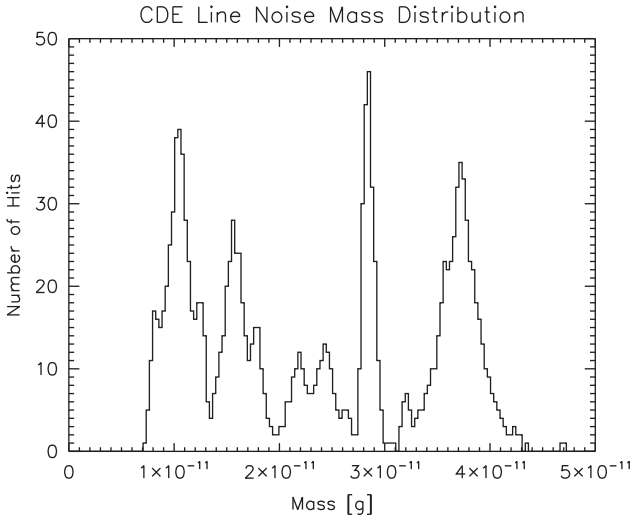

Fig. 7. Mass distribution for a single noise line on channel 8. Note the presence of several independent Gaussian peaks in the mass distribution.

that are not removed in the O1 analysis, by comparing all candidate hits to the characteristics of the individual lines identified as noise by O1. The first step is to identify, group, and characterize the coincident events belonging to each individual noise line. The lines are very regular spatially (see Fig. 2), facilitating the use of SZA as an index for discerning an individual line. Additionally, each event on the instrument, whether dust or noise, is given an equivalent mass based on the amplitude of the signal generated. Using these amplitudes, the differential mass distribution for each individual line is computed. The analysis of the line noise amplitude distributions shows that a single line often has multiple, independent amplitude peaks. An example of the amplitude distribution of one line on channel 8 is shown in Fig. 7. The mean and standard deviation in mass for all Gaussian mass peaks for each line are computed. Additionally, the mean and standard deviation in SZA are computed for the entire line. The combination of the SZA mean and standard deviation and the Gaussian fits to the noise amplitude distribution is used to characterize each line uniquely.

In order to distinguish between candidate hits that are noise events from candidate hits that are more likely dust impacts, each candidate hit is compared to the characteristics of the nearest line.

This comparison is made by using the location and noise amplitude fits of each line. The average and standard deviation of the SZA of the nearest line are used to determine the number of deviations in SZA that the candidate hit is from the nearest line. This value, σ_{SZA}, given by the equation

$$\sigma_{SZA} = \frac{|\alpha_{hit} - \alpha_{avg}|}{\sigma_{line,SZA}}, \tag{2}$$

where α_{hit} is the solar zenith angle of the candidate hit, α_{avg} is the average solar zenith angle of the nearest noise line and $\sigma_{line,SZA}$ is the standard deviation of the solar zenith angle of the line. Similarly, the mass of the candidate hit is compared to the mass distribution of the line, yielding the deviation for the candidate hit mass from the center of the nearest Gaussian mass peak of the line, σ_{mass}, given by

$$\sigma_{mass} = \frac{|m_{hit} - m_{avg}|}{\sigma_{line,mass}} \tag{3}$$

where m_{hit} is the mass of the candidate hit, m_{avg} is the average mass of the nearest noise line and $\sigma_{line,mass}$ is the standard deviation of the noise line mass amplitude. An overall index for the candidate hit is obtained by adding the two independent characteristics, σ_{SZA} and σ_{mass}, in quadrature:

$$\sigma_{total} = \sqrt{\sigma_{SZA}^2 + \sigma_{mass}^2} \tag{4}$$

This value is calculated for all the candidate hits, thereby assigning each a probability of belonging to a particular noise line rather than begin a dust impact. Events with low σ_{total} values are more likely noise, while events with large σ_{total} values are more likely to be dust impacts.

Once the σ_{total} parameter has been calculated for all candidate hits, a cutoff in σ_{total} must be established for each channel, where hits with σ_{total} values lower than the cutoff are considered noise and hits with σ_{total} values higher than the cutoff are considered dust impacts. To obtain the σ_{cutoff} for each channel, the flux for each channel is computed as a function of σ_{cutoff}, where hits with σ_{total} values below σ_{cutoff} are excluded from the calculation. A fit is made to the cumulative flux curve for each channel with the sum of two different functions, one representing the expected noise distribution and the other representing the expected dust distribution as a function of σ_{total}. For the noise, the distribution is assumed to be Gaussian with respect to σ_{total}:

$$\Gamma_{noise} \propto \exp(-\sigma_{total}^2). \tag{5}$$

The dust is assumed to be independent of the σ_{cutoff} parameter, and thus the distribution should be a negatively sloped line:

$$\Gamma_{dust} = a - b\sigma_{total}. \tag{6}$$

The sum of these two distribution functions is fit to the flux from each channel as a function of σ_{total}. An example of this type of fit is shown in Fig. 8 for channel 2. The σ_{cutoff} value for each channel

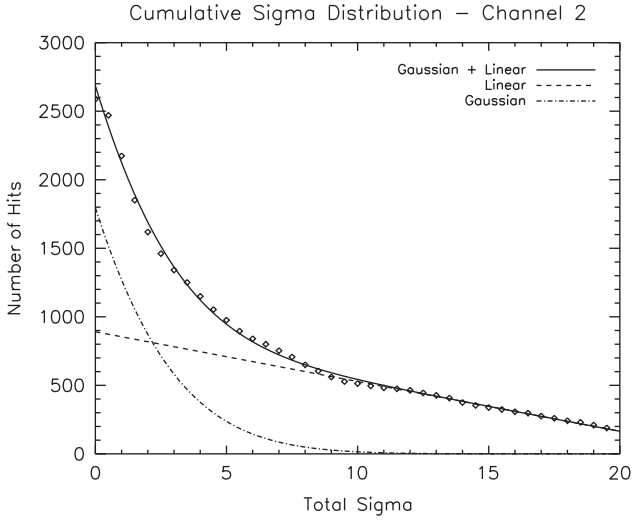

Fig. 8. Cumulative flux for channel 2 as a function of σ_{total}. Also shown is the sum of the Gaussian and linear fits, as well as the individual linear and Gaussian terms.

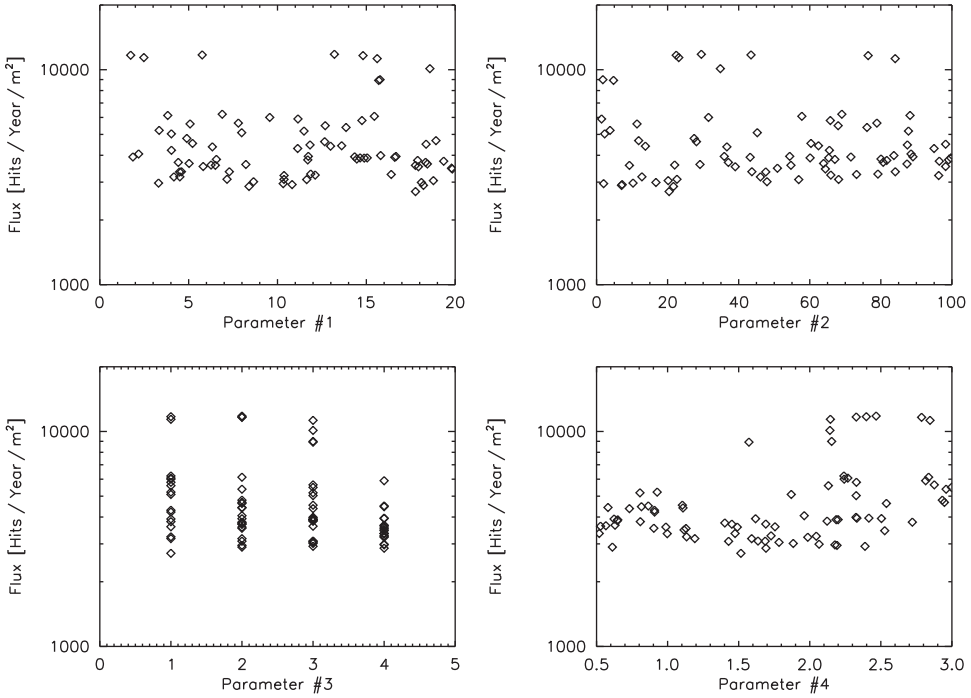

Fig. 9. Globally averaged influx for $r > 1.5$ μm as a function of the four parameters studies in the Monte Carlo algorithm analysis. The parameters are: (1) the number of days around a candidate hit with which to compare to the nearest noise line; (2) the relative weighting between the σ_{lat} and σ_{mass} values; (3) the number of bins surrounding a peak in the mass distribution with which a Gaussian curve is fit; and (4) the number of relative deviations above the mean mass of a line needed to qualify data as a mass peak. Note the discrete nature of parameter 3.

is determined by the location where the noise portion of the fit falls below 10% of the dust distribution. The candidate hits with $\sigma_{total} < \sigma_{cutoff}$ are removed and the remaining hits are identified as the true dust influx signal.

The non-standard nature of the noise algorithm used to extract the dust signal prevents a classical error analysis. Therefore, a detailed study was undertaken of the noise algorithm to quantify its reliability. Our algorithm has four free critical parameters: (1) the number of days around a candidate hit with which to compare to the nearest noise line; (2) the relative weighting between the σ_{SZA} and σ_{mass} values when calculating σ_{total}; (3) the number of bins surrounding a peak in the mass distribution with which a Gaussian curve is fit; and (4) the number of relative deviations above the mean mass of a line needed to qualify data as a mass peak. A Monte Carlo analysis was used to verify the sensitivity of our results to these parameters. One hundred random quartets of the parameters were generated and repeatedly run through the entire analysis code. Fig. 9 shows the total flux for grains with radius, $r > 1.5$ μm, as a function of each of the four input parameters, indicating no correlation of the dust flux with any of the parameters. Therefore, the spread in the reported flux values is simply indicative of the statistical accuracy of the algorithm.

Having eliminated the major noise sources via the algorithms presented above, the leftover events across all channels were considered to be dust impacts on the detectors. While the noise reduction has necessarily introduced additional error in the analysis, the measurement of the terrestrial cosmic dust influx, along with any associated spatial and/or temporal variability, was undertaken and is discussed in Section 6.

6. Temporal and spatial variability of the terrestrial cosmic dust influx

Fig. 10 shows the flux for each individual channel for grains with radius, $r > 1.5$ μm. The average flux across science detectors is $4.9 \pm 5.5 \times 10^3\ \mathrm{m^{-2}\,yr^{-1}}$ (note that channels 7 and 14 are the background channels and that during this time period, channel 14 measured no impacts with radius, $r > 1.5$ μm). The variation among channels is indicative of the variation in noise patterns affecting each channels. The average flux measured can also be

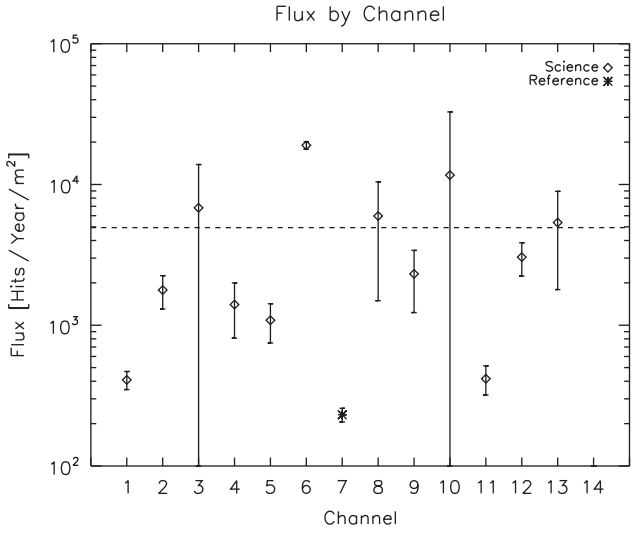

Fig. 10. Globally averaged influx for each channel for $r > 1.5$ μm. Science and reference channels are displayed as diamonds and stars, respectively, and the average flux across channels is shown as a dashed line. The error bars represent the variability from the Monte Carlo analysis for each individual channel. Note that channel 14 did not record any hits.

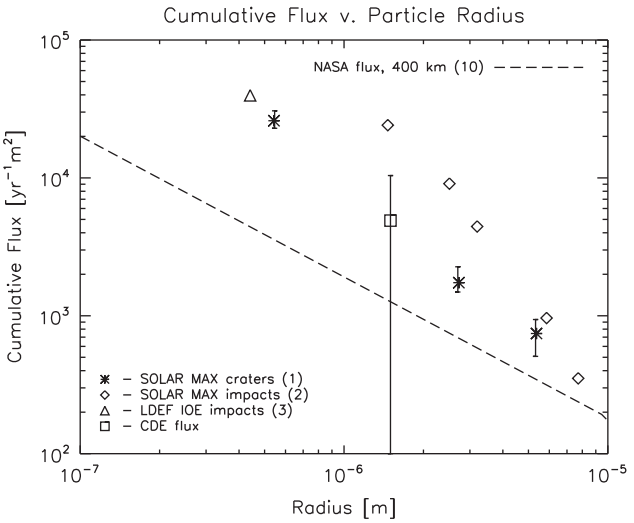

Fig. 11. Comparison of the mean CDE flux for grains, $r > 1.5$ μm with previous terrestrial dust measurements. For legend references, refer to the caption of Fig. 1.

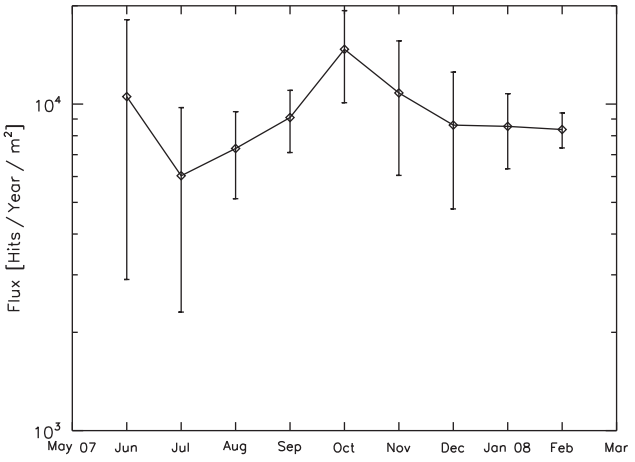

Fig. 12. Monthly averated dust fluxes for particles with radius $r > 1.5$ μm, between June 2007 and February 2008. The error bars represent variability from the Monte Carlo analysis.

compared to previous flux measurements (reported in full in Fig. 1) in Fig. 11. Despite the large amounts of noise across all detectors on the instrument, the reduced data show an averaged flux that is consistent with previous measurements.

One of the main goals of CDE is to measure the temporal and spatial variability of the cosmic dust input. Fig. 12 shows the globally averaged flux for $r > 1.5$ μm at monthly intervals. While the error bars remain relatively high, there is evidence of variability throughout the year on the order of a factor of two. Shown in Fig. 13, the northern hemisphere flux shows a peak around the time of the fall equinox, when the northern hemisphere is most pointed in the Earth's ram direction. Conversely, the southern hemisphere flux shows the beginning of a peak near the vernal equinox, however, the full annual cycle could not be presented due to the safing of the AIM spacecraft in February 2008.

The spatial variability of the terrestrial cosmic dust influx is detailed in Fig. 14, where the flux is plotted against the solar zenith angle, α, in 30° bins. The solar zenith angle is measured from the sub-solar point, with 90° and −90° representing the north and south ecliptic poles, respectively. The northern hemisphere noise discussed earlier has prevented analysis of any data within

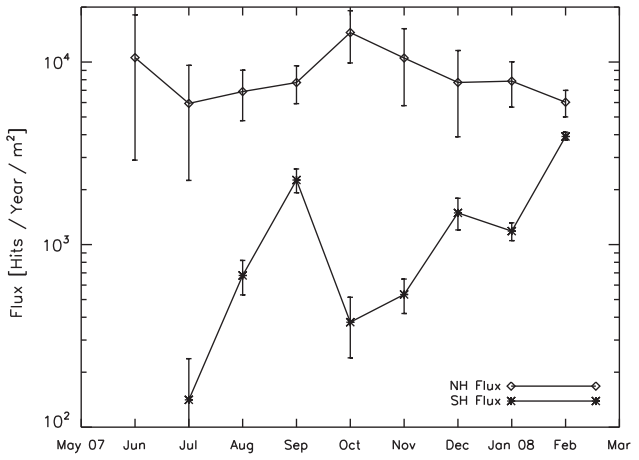

Fig. 13. Dust flux time series for the northern and southern hemispheres. (Note that no flux was measured in the southern hemisphere in June 2007.)

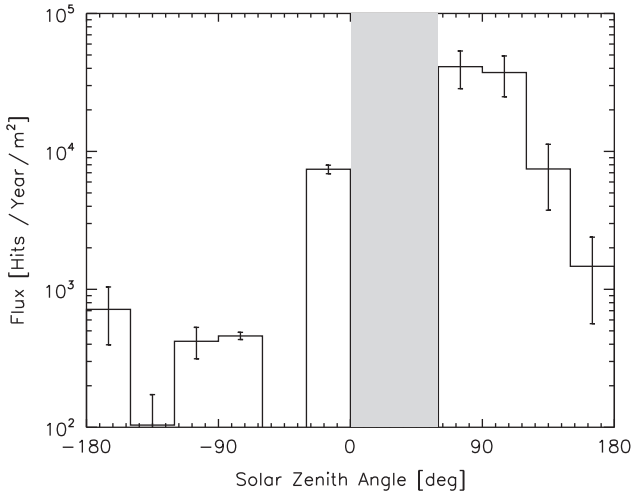

Fig. 14. Temporally averaged latitudinal flux distribution for particles with radius $r > 1.5$ μm, between June 2007 and February 2008. The error bars represent variability from the Monte Carlo analysis. Saturation from noise events prevented analysis between $-10^\circ < \alpha < 60^\circ$, shown as the grayed portion in the plot.

the region, $-10^\circ < \alpha < 60^\circ$. The data show a distinct anisotropy between the northern and southern hemispheres, with the flux entering the northern hemisphere at least an order of magnitude higher than that in the southern hemisphere. This is possibly due to observational limitations, in that the data presented here do not encompass an entire year. It is possible that the southern hemispheric time series peaks during the vernal equinox and thereby balances out the observed latitudinal anisotropy. Previous work including both observation and modeling has predicted such large-scale variability in the sporadic micrometeorite background (Janches et al., 2006). Unfortunately, due to the limited observation time, CDE cannot confirm or deny such a model, although the data do outline a picture consistent with previous work.

7. Conclusion

Measurements of the terrestrial micrometeorite input flux over eight months by the Cosmic Dust Experiment on the Aeronomy of Ice in the Mesosphere satellite have been reported. Several noise sources impeded a straightforward analysis of the CDE impact events and precipitated the development of a noise reduction algorithm in order to ascertain the true dust flux. The main noise sources were (1) events generated by the increasing capacitance mis-match of the detectors when heated by direct exposure to sunlight in the northern hemisphere (termed 'northern hemisphere noise') and (2) events most likely generated by sharp acoustic vibrations during the expansion and/or contraction of nearby spacecraft components. The northern hemisphere noise saturated the instrument and prevented any analysis of the input flux in the region $-10^\circ < \alpha < 60^\circ$. The noise generated by thermal mis-match of components was filtered out of the data by comparing candidate hits to those events identified as composing noise lines.

The cosmic dust flux measured by CDE showed variability in both space and time, consistent with other experimental measurements (Janches et al., 2006). The main component of the variability, both in time and space, is most likely due to the gradually changing angle between the Earth's ram direction (velocity vector about its orbit) and the observation area of the instrument. For example, during the northern hemisphere summer, CDE is preferentially pointed into the ram direction while over the northern hemisphere, yielding a local increase in the terrestrial dust influx. While not directly observed, the CDE data suggest a similar effect in the southern hemisphere during the southern hemisphere summer.

The time- and space-resolved measurements of the terrestrial cosmic dust input presented here should help constrain the role and impact that micrometeorite ablation in the mesosphere has on various phenomena such as PMC, PMSE and sporadic metallic layers. While previous studies of mesospheric phenomena have assumed a spatially isotropic influx of micrometeorites (Kalashnikova et al., 2000; Gabrielli et al., 2004; Megner et al., 2008; Bardeen et al., 2008), such broad variation in the dust influx as measured by CDE could have significant effects on the final results of such simulations.

While CDE has contributed to the understanding of the terrestrial dust influx by measuring its mean value and variability, there is much more to explore, including the full annual variability and mass distribution. Due to the relatively low dust fluxes, the development of instruments with large surface areas (≥ 0.1 m^2) will be required to make reliable measurements. Despite the levels of background noise detected by CDE, PVDF-type detector systems remain good candidates due to their modest cost, mass, and power resource requirements. The thermal issues experienced by CDE could be addressed by putting the instrument in a dawn-dusk low Earth orbit, and also by developing a more robust onboard capability to reject noise by analyzing the entire waveform of the registered events to identify true impact-generated signals. Additionally, PVDF dust detectors could be improved to distinguish mass and impact velocity via use of advanced electronics to sample the entire signal waveform; however, continued ground development of these detectors is required to implement any of these improvements.

Acknowledgements

This research was supported by the NASA Aeronomy of Ice in the Mesosphere, Small Explorer Mission. We thank the AIM PI, Dr. James M. Russell III, and the entire Science Team for their patience and encouragement through the years. We thank V. Hoxie, M. Lankton and S. Batiste for several discussions regarding the analysis of this data as well as the staff at the Dust Accelerator Facility at the Max Planck Institute for Nuclear Physics in Heidelberg, Germany, especially E. Grün and R. Srama, for their help in calibrating the CDE detectors.

References

Bardeen, C.G., Toon, O.B., Jensen, E.J., Marsh, D.R., Harvey, V.L., 2008. J. Geophys. Res. 113.

Bernhard, R.P., See, T.H., Hörz, F., In: LDEF: 69 Months in Space, pp. 551–573.
Cho, J.Y.N., Kelley, M.C., 1993. Rev. Geophys. 13, 243–265.
Cho, J.Y.N., Röttger, J., 1997. J. Geophys. Res. 102, 2001–2020.
Cziczo, D.J., Thomson, D.S., Murphy, D.M., 2001. Science 291, 1772–1775.
Fentzke, J.T., Janches, D., 2008. J. Geophys. Res. 113.
Gabrielli, P., et al., 2004. Nature 432, 1011–1014.
Gleghorn, G., Asay, J., Atkinson, D., Flury, W., Johnson, N., Kessler, D., Knowles, S., Rex, D., Toda, S., Veniaminov, S., 1995. Orbital Debris: A Technical Assessment. National Academy Press.
Goldstein, R.M., Randolph, L.W., 1992. IEEE Trans. Microwave Theory Tech. 40, 1077–1080.
Gordley, L., Hervig, M., Fish, C., III, J.M.R., Cook, J., Hanson, S., Shumway, A., Bailey, S., Paxton, G., Deaver, L., Marshall, T., Burton, J., Magill, B., Brown, C., Thompson, E., Kemp, J., 2008. J. Atmos. Solar-Terr. Phys 71, 300–315.
Horányi, M., et al., 2008. Space Sci. Rev 140, 387–402.
Humes, D.H., In: LDEF: 69 Months in Space, pp. 287–322.
Hunten, D.M., Turco, R.P., Toon, O.B., 1980. J. Atmos. Sci. 37, 1342–1357.
Hörz, F., Brownlee, D.E., Fechtig, H., Hartung, J.B., Morrison, D.A., Neukum, G., Schneider, E., Vedder, J.F., Gault, D.E., 1975. Planet. Space Sci. 23, 151–172.
James, D., Horányi, M., Hoxie, V., 2010. Rev. Sci. Instrum. 81.
Janches, D., Chau, J.L., 2005. J. Atmos. Solar-Terr. Phys. 67.
Janches, D., ReVelle, D.O., 2005. J. Geophys. Res. 110.
Janches, D., Nolan, M.C., Meisel, D.D., Mathews, J.D., Xhou, Q.H., Moser, D.E., 2003. J. Geophys. Res. 108.
Janches, D., Heinselman, C.J., Chau, J.L., Chandran, A., Woodman, R., 2006. J. Geophys. Res. 111.
Jessberger, E.K., Stephan, T., Rost, D., Arndt, P., Maetz, M., Stadermann, F.J., Brownlee, D.E., Bradley, J.P., Kurat, G., 2001. In: Grün, E., Interplanetary Dust, Springer-Verlag.
Kalashnikova, O., Horányi, M., Thomas, G.E., Toon, O.B., 2000. Geophys. Res. Lett. 27, 3293–3296.
Laurance, M.R., Brownlee, D.E., 1986. Nature 323, 136–138.
Leinert, C., 1975. Space Sci. Rev. 18, 281–339.
Love, S.G., Brownlee, D.E., 1991. Icarus 89, 26–43.
Love, S.G., Brownlee, D.E., 1993. Science 262, 550–553.
Lübken, F.-J., Rapp, M., 2001. J. Atmos. Solar-Terr. Phys. 63, 771–780.
Mathews, J.D., Janches, D., Meisel, D.D., Zhou, Q.-H., 2001. Geophys. Res. Lett. 28, 1929–1932.
Megner, L., et al., 2008. J. Geophys. Res. 113.
Murphy, D.M., Thomson, D.S., Mahoney, M.J., 1998. Science 282.
Nalwa, H.S., 1995. Ferroelectric Polymers. Marcel Dekker, Inc.
Plane, J.M.C., 2003. Chem. Rev. 103, 4963–4984.
Poppe, A., James, D., Jacobsmeyer, B., Horányi, M., 2010. Geophys. Res. Lett. 37.
Poppe, A., Jacobsmeyer, B., James, D., Horányi, M., 2010. Nucl. Instrum. Methods A 622, 583–587.
Radeka, V., 1974. IEEE Trans. Nucl. Sci. 21.
Rapp, M., 2009. Ann. Geophys. 27.
Rapp, M., Lübken, F.-J., 2001. J. Atmos. Solar-Terr. Phys. 63, 759–770.
Rapp, M., Thomas, G.E., 2006. J. Atmos. Solar-Terr. Phys. 68, 715–744.
Rusch, D., Thomas, G.E., McClintock, W., Merkel, A., Bailey, S., III, J.M.R., Randall, C., Jeppesen, C., Callan, M., 2009. J. Atmos. Solar-Terr. Phys 71, 356–364.
Russell, J.M., Bailey, S., Horányi, M., Gordley, L., Rusch, D., Hervig, M., Thomas, G.E., Randall, C., Siskind, D., Stevens, M., Summers, M., Taylor, M., Englert, C., Espy, P., McClintock, W., Merkel, A., 2009. J. Atmos. Solar-Terr. Phys 71, 289–299.
Schwanenthal, J.P., 2004. Debris in-orbit evaluator (DEBIE) calibration and data analysis. Ph.D. Thesis, The Open University.
Simon, C.G., Mulholland, J.D., Oliver, J.P., Cooke, W.J., Kassel, P.C., In: LDEF: 69 Months in Space, pp. 693–703.
Simpson, J.A., Tuzzolino, A.J., 1985. Nucl. Instrum. Methods A 236, 187–202.
Sparks, J.J., Janches, D., 2009. Geophys. Res. Lett. 36.
Spieler, H., 2005. Semiconductor Detector Systems. Oxford University Press, New York.
Srama, R., et al., 2004. Space Sci. Rev. 114, 465–518.
Stansbery, E.G., Kessler, D.J., Tracy, T.E., Matney, M.J., Stanley, J.F., 1995. Adv. Space Res. 16, 5–16.
Sulzer, M.P., 2004. Atmos. Chem. Phys. 4, 947–954.
Thompson, T.W., Goldstein, R.M., Campbell, D.B., 1992. Geophys. Res. Lett. 19, 257–259.
Turco, R.P., Toon, O.B., Hamill, P., Whitten, R.C., 1981. J. Geophys. Res. 86, 1113–1128.
Turco, R.P., Toon, O.B., Whitten, R.C., Keesee, R.G., Hollenbach, D., 1982. Planet. Space Sci. 30, 1147–1181.
Tuzzolino, A.J., 1992. Nucl. Instrum. Methods A 316, 223–237.
Tuzzolino, A.J., et al., 2001a. Planet. Space Sci. 49, 689–703.
Tuzzolino, A.J., et al., 2001b. Planet. Space Sci. 49, 705–729.
Tuzzolino, A.J., et al., 2004. Science 304, 1776–1780.